AMPLITUDE ENGINEERING FOR BEAMFORMERS WITH SELF-BENDING DIRECTIVITY BASED ON CONVEX OPTIMIZATION

Jens Ahrens

Audio Technology Group, Division of Applied Acoustics
Chalmers University of Technology, 412 96 Gothenburg, Sweden
jens.ahrens@chalmers.se

ABSTRACT

Arrays producing self-bending beams were proposed in the literature recently. The self-bending property of the beam is achieved by matching the phase profile that is applied to the array elements to a self-bending wave field. This process is termed phase engineering. It has been unclear how the optimal amplitude profile can be determined as the amplitude distribution of a self-bending wave field is difficult to determine. Previous works employed educated guesses. In this paper, we apply convex optimization to perform amplitude engineering. In other words, we complement phase engineering by determining the purely real amplitude weights that minimize the norm of the amplitude weights for a given maximum beam amplitude in the dark zone around which the beam bends. We show that phase engineering by itself does not narrow down the solution space sufficiently so that the choice of control points in the dark zone has a significant impact on how well the desired self-bending property forms.

Index Terms— Phase engineering, beamforming, convex optimization, Airy beams

1. INTRODUCTION

Self-bending wave fields were first predicted in the field of quantum mechanics [1] and made their way to acoustics via optics [2]. In optics, a phase profile is imposed onto a beam of light via a phase mask, e.g. a transparent material of appropriately varying thickness [3]. The phase profile that is imposed is taken from an optical wave front that forms a caustic. A caustic occurs if the family of rays that represent the wave front exhibit an envelope and are tangent to that envelope. This envelope is then referred to as caustic. The same concept was applied to acoustic fields by [4, 5] using an array of acoustic transducers that controlled the phase profile of the evolving sound field.

The literature mentioned above focuses on the creation of self-bending wave fields. The application of the concept to sensor arrays to achieve a self-bending sensitivity was proposed in [6], which opens a new line of conceivable practical implementations. The mechanisms for creating self-bending waves and self-bending sensitivities are essentially identical due to the reciprocity of the Helmholtz equation. We will simply speak of self-bending beams in the remainder of this paper, which refers to both cases.

Either way, the resulting beams exhibit distance dependent properties. A closely related domain is nearfield beamforming, where a distance-dependent beam is typically achieved by taking the curvature differences between planar and spherical waves into account [7, 8, 9, 10]. Both the gain and the delay (or, equivalently, the complex weights) are determined for each of the array elements.

The extent to which physical limitations are taken into account in nearfield beamforming is typically limited so that robustness is achieved by regularization, which comes at the price of a reduction in the performance that is difficult to control. In the present paper, we present a numerical solution for the creation of self-bending beams that uses a phase profile that is determined via physical considerations, and employs optimization only for the purely real amplitude weights. This way, we are incorporating more physical knowledge into the solutions than purely signal processing-based solutions are.

2. SELF-BENDING WAVE FRONTS

Self-bending wave fields are essentially fields that are composed of wave fronts that fold along a caustic. As the Airy integral developed in the 1930s by Sir George Biddell Airy is a powerful tool for explaining caustics, such waves are termed *Airy wavepackets* or *Airy beams* in electromagnetics and in optics.

Obviously, the wave itself is not accelerated. Rather, the amplitude envelope of the wave field appears to be bent. The concept of [4, 5] is illustrated in Fig. 1(a): A caustic is pre-defined along which the wave front folds. In the high-frequency limit, the wave front does not traverse the caustic. It is important to note that self-bending waves evolve only in the high-frequency limit. This high-frequency limit is fulfilled if the considered wavelength is much smaller than the curvature of the caustic. More generally, any significant changes to the wave amplitude have to evolve at length scales much larger than the wavelength. Note that the caustic needs to be convex in order that the wave perfectly avoids a given region in the high-frequency limit.

We choose the sample caustic from [4, 6], which is given by the cubic Bézier curve

$$B(t) = (1-t)^3 B_0 + 3t(1-t)^2 B_1 + 3(1-t)t^2 B_2 + t^3 B_3 \,, \quad (1)$$

with

$$B_0 = [0, -0.2311]^T, \qquad B_1 = [0.1, 0.0189]^T$$
$$B_2 = [0.25, 0.1689]^T, \qquad B_3 = [0.98, -0.3311]^T \,,$$

to allow for a direct comparison of the results. We limit our observations to the x-y-plane so that we define the four points that define the Bézier curve as $B_i = [x_i, y_i, 0]^T$. The red line in Fig. 1(a) illustrates (1). Note that the control variable t does not represent the traveled distance along $B(t)$, nor is it directly proportional to time when a wave moves along $B(t)$.

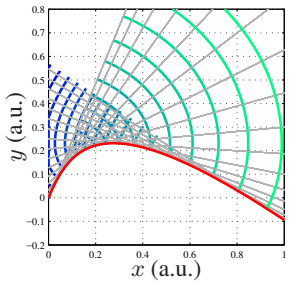

(a) Schematic of the principle of self-bending wave fronts via rays; the red line indicates the prescribed caustic given by (1); the gray lines are sample tangents of the caustic; the blue/green lines are sample wave fronts; time may evolve from blue to green as well as from green to blue

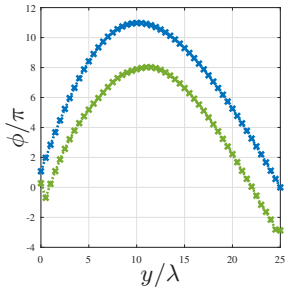

(b) Unwrapped phase profile $\phi(\cdot)$ of the arrays depicted in Fig. 2; caustic based (blue curve); numeric solution (green curve)

Figure 1: Schematic of a caustic and corresponding phase profiles

3. CREATION OF SELF-BENDING WAVES

As proven by, for example, Rayleigh's first integral formula, a wave field can be synthesized if its directional gradient is known along a reference plane and if there is a continuous distribution secondary monopole sources along this reference plane [11]:

$$P(\mathbf{x},\omega) = \iint_{-\infty}^{\infty} \underbrace{2\frac{\partial}{\partial \mathbf{n}} S(\mathbf{x},\omega)\big|_{\mathbf{x}=\mathbf{x}_0}}_{=D(\mathbf{x}_0,\omega)} G(\mathbf{x}_0,\mathbf{x},\omega) d\Omega(\mathbf{x}_0)\ . \quad (2)$$

$P(\cdot)$ denotes the harmonic scalar wave field that evolves due to the monopole distribution along the reference plane. $G(\mathbf{x},\mathbf{x}_0,\omega) = \frac{1}{4\pi}\frac{e^{-\mathrm{i}\omega/c|\mathbf{x}-\mathbf{x}_0|}}{|\mathbf{x}-\mathbf{x}_0|}$ is the free-field Green's function, i.e. the spatio-temporal transfer function of the secondary monopole sources. $S(\cdot)$ is an arbitrary virtual scalar wave field that is source-free in the target half-space that is bounded by the reference plane. $d\Omega(\cdot)$ is an infinitesimal surface element. $\mathbf{x}_0$ is a position on the reference plane.

When the secondary monopoles are driven with two times the gradient $\partial/\partial\mathbf{n}$ of $S(\cdot)$ in direction normal to the boundary and evaluated at the boundary, then the synthesized wave field $P(\cdot)$ is identical to the virtual (prescribed) field $S(\cdot)$ inside the target half-space. It is proven in the Appendix that the phase profile $\angle D(\cdot)$ of the driving signal is identical to the phase $\phi(\mathbf{x}_0,\omega)$ of the harmonic field at the positions of the secondary sources. It is therefore possible to create a self-bending wave by imposing the back traced phase profile of the self-bending wave onto a planar array of sufficiently densely spaced transducers. This approach is termed *phase engineering* [4, 5].

Eq. (6) in the Appendix also shows that the purely real gain (or *amplitude profile*) $|D(\cdot)|$ of the secondary sources is given by $A(\mathbf{x}_0,\omega)\phi'(\mathbf{x}_0,\omega)$, whereby $A(\cdot)$ is the amplitude distribution of the self-bending field along the reference plane, The prime $'$ represents spatial differentiation.

4. LINEAR ARRAYS

Planar transducer arrays are inconvenient as the required number of elements is high. When wave field synthesis inside a given plane is targeted, then also linear arrays may be employed. The driving functions $D(\cdot)$ are identical to those for planar arrays apart from a global frequency dependent factor. This type of scenario is termed 2.5-dimensional and is well known in sound field synthesis [12]. The curvatures of the wave fronts that evolve are identical to the prescribed ones inside the target half-plane. The control over the amplitude decay of the synthesized field over distance to the array is limited. The synthesized wave field is obviously invariant with respect to rotation about the axis through the array's elements.

For convenience, we assume a linear array of transducers here. Due to the reciprocity of the Helmholtz equation, we may interpret the beam as the amplitude distribution of the synthesized sound field (when loudspeakers are assumed) or as amplitude distribution of the array's sensitivity (when microphones are assumed).

5. OPTIMAL ARRAY PATTERN SYNTHESIS

A vast amount of literature exists on numerically optimal array pattern synthesis in the domain of beamforming both for signal-dependent scenarios as well as for the present case of signal-independent scenarios [13]. A variety of optimality criteria exist. A typical criterion for signal-independent farfield scenarios is maximizing the so-called white noise gain (WNG) [14], which represents the gain of the target signal (i.e., the desired signal) that the beamformer achieves relative to spatially white noise. A convex solution incorporating a constraint on the WNG of a farfield beamformer is presented in [15]. This scheme is not convenient in the present case as it is inconvenient to define what is the location of the target signal as there are many useful options.

We therefore adapt the approach that is typically applied in nearfield beamforming: We assume a discrete set of array elements and find the set of weights $D(\mathbf{x}_0,\omega)$ that minimize the beam amplitude in the dark zone (signals from which are intended to be suppressed) while maintaining unit amplitude at the target location [7]. This can lead to very aggressive and therefore non-robust solutions, which are not applicable when the actual array exhibits the slightest deviations from the assumptions. A lack of robustness is typically an indication for a large range of gains of the array elements. Regularization can be applied, which modifies the solution in order to squash this range at the expense of an (uncontrolled) reduction in performance.

We employ the convex approach from [16] here in which we specify the performance and aim at finding the set of gains with the lowest norm $\|D(\cdot)\|$ that enables the desired performance. $D(\cdot)$ is the vector containing the weights of all (discrete) array elements. Searching for the lowest norm inherently squashes the range of weights with relaxation of the performance requirements.

More explicitly, the present optimization problem reads

$$\min \|D(\mathbf{x}_0,\omega)\| \quad (3)$$

subject to

$$\mathbf{G}(\mathbf{x}_0,\mathbf{x}_t,\omega)D(\mathbf{x}_0,\omega) = 1, \quad (3a)$$

$$|\mathbf{G}(\mathbf{x}_0,\mathbf{x}_d,\omega)D(\mathbf{x}_0,\omega)| \leq 10^{\frac{C}{20}} \quad (3b)$$

whereby C denotes the desired attenuation in dB at the control points in the dark zone relative to the target location in the bright

zone.

$$\mathbf{G}(\mathbf{x}_0, \mathbf{x}_t, \omega) = \begin{bmatrix} e^{-\mathrm{i}\phi_1(\omega)} G(\mathbf{x}_{0,1}, \mathbf{x}_t, \omega) \\ e^{-\mathrm{i}\phi_2(\omega)} G(\mathbf{x}_{0,2}, \mathbf{x}_t, \omega) \\ \vdots \\ e^{-\mathrm{i}\phi_N(\omega)} G(\mathbf{x}_{0,N}, \mathbf{x}_t, \omega) \end{bmatrix}^T$$

is a vector containing the transfer paths from the N individual array elements indexed by n to the target location in the bright zone, and

$$\mathbf{G}(\mathbf{x}_0, \mathbf{x}_d, \omega) = \begin{bmatrix} e^{-\mathrm{i}\phi_1(\omega)} G(\mathbf{x}_{0,1}, \mathbf{x}_{d,1}, \omega) & \dots & e^{-\mathrm{i}\phi_N(\omega)} G(\mathbf{x}_{0,N}, \mathbf{x}_{d,1}, \omega) \\ e^{-\mathrm{i}\phi_1(\omega)} G(\mathbf{x}_{0,1}, \mathbf{x}_{d,2}, \omega) & \dots & e^{-\mathrm{i}\phi_N(\omega)} G(\mathbf{x}_{0,N}, \mathbf{x}_{d,2}, \omega) \\ \vdots & \vdots & \vdots \\ e^{-\mathrm{i}\phi_1(\omega)} G(\mathbf{x}_{0,1}, \mathbf{x}_{d,M}, \omega) & \dots & e^{-\mathrm{i}\phi_N(\omega)} G(\mathbf{x}_{0,N}, \mathbf{x}_{d,M}, \omega) \end{bmatrix}$$

is a matrix containing the transfer paths from the N individual array elements to the M control points in the dark zone. Note that we search for purely real $D(\cdot)$. The phase engineering is performed by incorporating the phase profile $\phi(\mathbf{x}_0, \omega)$ into the transfer paths $\mathbf{G}(\mathbf{x}_0, \mathbf{x}_d, \omega)$.

6. RESULTS

Refer to Fig. 2 for sample monochromatic self-bending beams based on the caustic that is defined by (1) and depicted in Fig. 1(a). The array of isotropic (monopole) elements extends along the y-axis. The blue curve in Fig. 1(b) depicts the phase profile that was imposed on the array elements. Fig. 2(a) shows the resulting beam amplitude when all array elements exhibit equal amplitude. This corresponds to the approaches presented in [4, 5]. The attenuation in the quiet zone is in the order of 20 dB compared to locations along the caustic. Fig. 2(b) shows the resulting beam when a cosine-squared shaped weighting as illustrated by the blue curve in Fig. 3 is imposed on the array elements. The difference to Fig. 2(a) is eminent [6]. A pronounced quiet zone evolves south of the caustic indicated by the black line. The attenuation in the quiet zone is in the order of 60 dB or more compared to locations along the caustic. Note that the cosine-squared shaped amplitude profile works well in the present scenario. But it cannot be considered a general solution.

Fig. 4 depicts the numerical solutions according to (3). All weight sets including the ones from Fig. 2(b) have been normalized to 1.

A remarkable observation is that although we are solving (3) for purely real weights, it is generally not such that all weights exhibit the same algebraic sign as our physical model of phase and magnitude would suggest it. (Note that a change in sign is equivalent to a phase jump by π.) All simulations presented in this paper therefore employed the condition that all real weight have to exhibit the same algebraic sign additional to the conditions (3a) and (3b).

Another important observation when comparing Fig. 4(a) and (b) is that the choice of control points has a fundamental effect on the spatial evolution of the beam. The mere prescription of a phase profile onto the array elements does not narrow down the solution space sufficiently. However, it seems unreasonable to sample the dark zone densely with control points. The contour in Fig. 4(b) is a shifted copy of a segment of the prescribed caustic and constitutes a useful choice. It prevents the beam from entering the dark zone. The resulting amplitude profile is given by the red curve in Fig. 3.

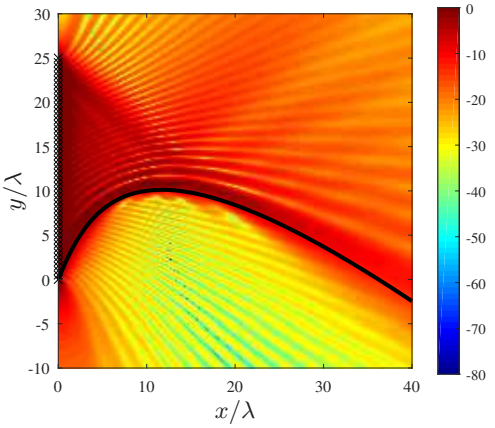

(a) Equal amplitude of 1 imposed on all array elements

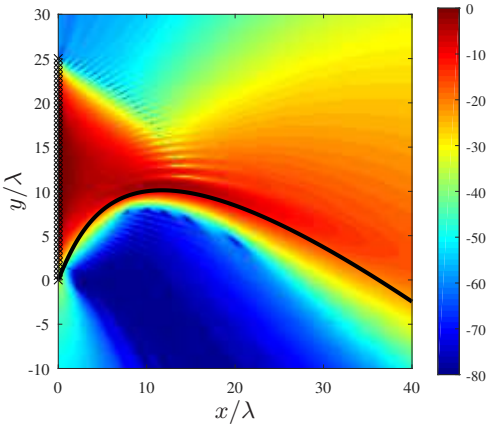

(b) Cosine-squared amplitude profile imposed on the array elements

Figure 2: Magnitude in dB of the beam of a sample linear array of 51 isotropic (omnidirectional) elements of length $L = 25\lambda$ located on the y-axis; the element spacing is $\Delta y = 0.5\lambda$; the black marks indicate the locations of the arr ay elements; the black line represents the caustic

Instead of solving (3) for purely real weights, we can, of course, also skip prescribing a phase profile and solve for complex weights. At first sight, we are thereby removing all physics from the problem. However, by using the same control points like in Fig. 4(b), we are inherently assuming the solution to be related to the modelled caustic. The result depicted in Fig. 4(c) is very comparable to Fig. 4(b). Bear in mind that we have two times the amount of variables to solve for (the real part as well as the imaginary part of the weights) so that we require two times as many control points. The corresponding amplitude and phase profiles are given by the green curves in Fig. 3 and Fig. 1(b), respectively.

Note that both the purely real as well as the complex solution do not necessarily require an overdetermined equation system as it has been chosen here. The requirements regarding the number and spacing of the control points will be studied in future work.

7. CONCLUSIONS

We present amplitude engineering for self-bending beamformers by prescribing an appropriate phase contour onto the elements of a lin-

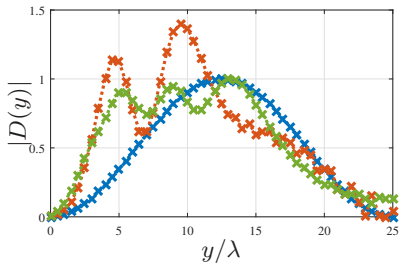

Figure 3: Amplitude profiles $\phi(\cdot)$ applied in Fig. 2(b) (blue curve), Fig. 4(b) (red curve), and Fig. 4(c) (green curve)

ear array and solving for the optimal purely real element gains that enable the desired attenuation in the dark zone around which the beam bends. We showed that the mere prescription of the phase profile is not necessarily yield the desired solution. The choice of control points is also essential.

The presented solution cannot be assumed to be a general one. We rather provided first results for further investigation on the choice of control points, conditions, and constraints for the solution.

The investigation of the robustness of the approach was beyond the scope of this paper. The reader is referred to the results from [6] obtained that were obtained with a cosine-squared window.

APPENDIX: DERIVATION OF THE SECONDARY SOURCE PHASE PROFILE

Consider the driving function $D(\mathbf{x}_0, \omega)$ for the secondary source at $\mathbf{x}_0$ to synthesize a sound pressure field $S(\mathbf{x}, \omega)$ as given by (2). The directional gradient $\frac{\partial}{\partial \mathbf{n}}$ is defined as [17]

$$\frac{\partial}{\partial \mathbf{n}} = \cos\alpha_\mathrm{n} \sin\beta_\mathrm{n} \frac{\partial}{\partial x} + \sin\alpha_\mathrm{n} \sin\beta_\mathrm{n} \frac{\partial}{\partial y} + \cos\beta_\mathrm{n} \frac{\partial}{\partial z} \,, \quad (4)$$

with α_n being the azimuth of the orientation of $\mathbf{n}$ and β_n being the colatitude. For the present case of $\mathbf{n}$ pointing in positive x-direction, $\partial/\partial\mathbf{n}$ simplifies to $\partial/\partial x$.

Recall that we assume stationary conditions and time-harmonic signals in this paper. We may express $S(\mathbf{x}, \omega)$ as

$$S(\mathbf{x}, \omega) = A(\mathbf{x}, \omega) e^{\mathrm{i}\phi(\mathbf{x},\omega)} \quad (5)$$

with purely real amplitude $A(\mathbf{x}, \omega) = |S(\mathbf{x}, \omega)|$ and purely real phase $\phi(\mathbf{x}, \omega) = \angle S(\mathbf{x}, \omega)$. Differentiation of (5) with respect to any of the Cartesian dimensions yields

$$\begin{aligned} \left(A(\mathbf{x},\omega)e^{\mathrm{i}\phi(\mathbf{x},\omega)}\right)' &= A'(\mathbf{x},\omega)e^{\mathrm{i}\phi(\mathbf{x},\omega)} + A(\mathbf{x},\omega)\left(e^{\mathrm{i}\phi(\mathbf{x},\omega)}\right)' \\ &= \left[A'(\mathbf{x},\omega) + A(\mathbf{x},\omega)\mathrm{i}\phi'(\mathbf{x},\omega)\right] e^{\mathrm{i}\phi(\mathbf{x},\omega)} \\ &\backsimeq A(\mathbf{x},\omega)\phi'(\mathbf{x},\omega)e^{\mathrm{i}\phi(\mathbf{x},\omega)+\mathrm{i}\frac{\pi}{2}} \,, \end{aligned} \quad (6)$$

where in the last step we made use of the stipulated assumption that the high-frequency limit applies, i.e. $\left|\frac{\partial}{\partial\mathbf{n}}A(\mathbf{x},\omega)\right| \ll \left|\frac{\omega}{c}\mathbf{n}A(\mathbf{x},\omega)\right|$, which is known as the *eikonal approximation* [18].

Recall that (2) states that $D(\mathbf{x}_0, \omega) \propto \left(A(\mathbf{x},\omega)e^{\mathrm{i}\phi(\mathbf{x},\omega)}\right)'|_{\mathbf{x}=\mathbf{x}_0}$. We can deduce from (6) that, in the high-frequency limit, the phase profile $\phi(\mathbf{x}_0, \omega)$ of the driving function $D(\mathbf{x}_0, \omega)$ is identical to the phase profile of the desired sound field on the secondary source contour and the term $A(\mathbf{x}, \omega)\phi'(\mathbf{x}, \omega)$ in (6) represents the (purely real) weight profile to be applied.

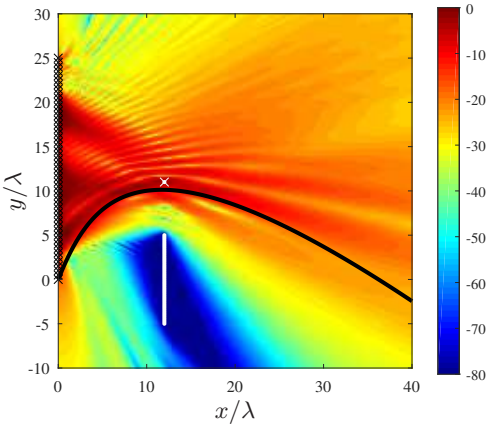

(a) Real weights and phase profile from Fig. 1(b); 52 control points were used (51 + 1)

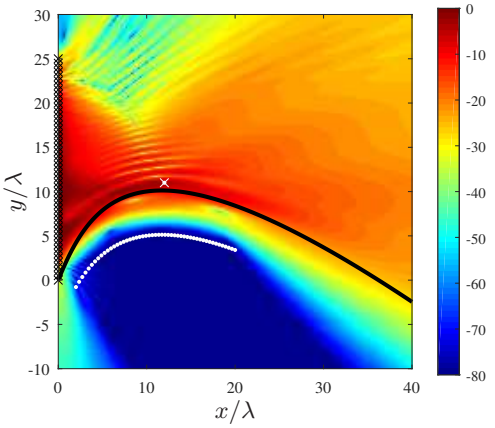

(b) Real weights and phase profile from Fig. 1(b); 52 control points were used (51 + 1)

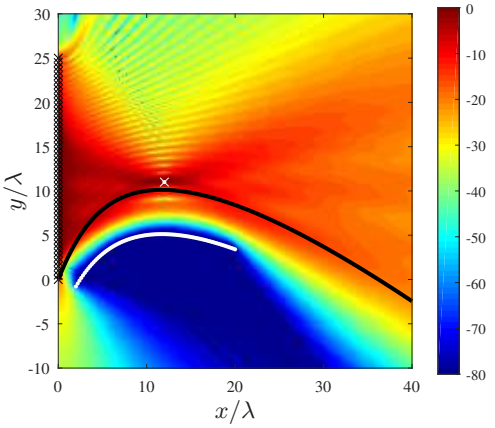

(c) Complex weights with no prescribed phase profile; 92 control points were used (91 + 1)

Figure 4: Magnitude in dB of the beams produced by the array from Fig. 2 using optimal solutions according to (3); $C = -80$ dB; the white cross marks the control point in the bright zone; the white points mark the control points in the dark zone

8. REFERENCES

[1] M. V. Berry and N. L. Balazs, "Nonspreading wave packets," *A. J. Phys.*, vol. 47, no. 3, pp. 264–267, Mar. 1979.

[2] G. A. Siviloglou and D. N. Christodoulides, "Accelerating finite energy Airy beams," *Optics Letters*, vol. 32, no. 8, Apr. 2007.

[3] E. Greenfield, M. Segev, W. Walasik, and O. Raz, "Accelerating light beams along arbitrary convex trajectories," *Phys. Rev. Lett.*, vol. 106, no. 213902, May 2011.

[4] P. Zhang, T. Li, J. Zhu, X. Zhu, S. Yang, Y. Wang, X. Yin, and X. Zhang, "Generation of acoustic self-bending and bottle beams by phase engineering," *Nature Communications*, vol. 5, no. 4316, pp. 1–9, 2014.

[5] S. Zhao, Y. Hu, J. Lu, X. Qiu, J. Cheng, and I. Burnett, "Delivering sound energy along an arbitrary convex trajectory," *Scientific Reports*, vol. 4, no. 6628, pp. 1–6, 2014.

[6] J. Ahrens, "A linear sensor array with self-bending sensitivity," in *IEEE International Conference on Acoustics, Speech and Signal Processing (ICASSP)*, March 2016.

[7] H. Lebret and S. Boyd, "Antenna array pattern synthesis via convex optimization," *IEEE Transactions on Signal Processing*, vol. 45, no. 3, pp. 526–532, Mar. 1997.

[8] R. Kennedy, T. Abhayapala, and D. Ward, "Broadband nearfield beamforming using a radial beampattern transformation," *IEEE Transactions on Signal Processing*, vol. 46, no. 8, pp. 2147–2156, 1998.

[9] J. R. Zheng, R. A. Goubran, and M. El-Tanany, "Robust near-field adaptive beamforming with distance discrimination," *IEEE Transactions on Speech and Audio Processing*, vol. 12, no. 5, pp. 478–488, Sept. 2004.

[10] E. Fisher and B. Rafaely, "Near-field spherical microphone array processing with radial filtering," *IEEE TASL*, vol. 19, no. 2, pp. 256–265, Feb. 2011.

[11] E. Williams, *Fourier Acoustics: Sound Radiation and Nearfield Acoustical Holography*. London, UK: Academic Press, 1999.

[12] J. Ahrens, *Analytic Methods of Sound Field Synthesis*. Berlin, Heidelberg: Springer-Verlag, 2012.

[13] H. L. van Trees, *Optimum Array Processing*. New York: Wiley, 2002.

[14] W. Herbordt, *Sound capture for human/machine interfaces*. Berlin, Heidelberg: Springer-Verlag, 2005.

[15] E. Mabande, A. Schad, and W. Kellermann, "Design of robust superdirective beamformers as a convex optimization problem," in *IEEE International Conference on Acoustics, Speech, and Signal Processing (ICASSP)*, March 2009.

[16] S. Boyd, "Convex optimization examples," Lecture notes (EE364), Stanford University, 2017.

[17] G. B. Arfken and H. J. Weber, *Mathematical Methods for Physicists*, 6th ed. Burlington, MA: Elsevier Academic Press, 2005.

[18] M. Born and E. Wolf, *Principles of Optics*, 4th ed. Oxford, UK: Pergamon Press, 1970.